



ELSEVIER

New Astronomy 3 (1998) 275–291

New Astronomy

Correlations between the cosmic X-ray and microwave backgrounds: constraints on a cosmological constant

S.P. Boughn^{a,b,1}, R.G. Crittenden^{c,2}, N.G. Turok^{d,3}^a*Institute for Advanced Study, Princeton, NJ 08540, USA*^b*Department of Astronomy, Haverford College, Haverford, PA 19041, USA*^c*CITA, University of Toronto, Toronto, Ontario M5S 3H8, Canada*^d*DAMTP, University of Cambridge, Cambridge CB3 9EW, UK*

Received 27 March 1997; accepted 9 March 1998

Communicated by Edmund Bertschinger

Abstract

In universes with significant curvature or cosmological constant, cosmic microwave background (CMB) anisotropies are created very recently via the Rees-Sciama or integrated Sachs-Wolfe effects. This causes the CMB anisotropies to become partially correlated with the local matter density ($z < 4$). We examine the prospects of using the hard (2–10 keV) X-ray background as a probe of the local density and the measured correlation between the HEAO1 A2 X-ray survey and the 4-year COBE-DMR map to obtain a constraint on the cosmological constant. The 95% confidence level upper limit on the cosmological constant is $\Omega_\Lambda \leq 0.5$, assuming that the observed fluctuations in the X-ray map result entirely from large scale structure. (This would also imply that the X-rays trace matter with a bias factor of $b_x \approx 5.6 \Omega_m^{0.53}$.) This bound is weakened considerably if a large portion of the X-ray fluctuations arise from Poisson noise from unresolved sources. For example, if one assumes that the X-ray bias is $b_x = 2$, then the 95% confidence level upper limit is weaker, $\Omega_\Lambda \leq 0.7$. More stringent limits should be attainable with data from the next generation of CMB and X-ray background maps. © 1998 Elsevier Science B.V.

PACS: 98.80.Es; 95.85.Nv; 98.70.Vc; 98.65-r

Keywords: Cosmic microwave background; X-rays: general; Large-scale structure of universe

1. Introduction

The recent observations of anisotropies in the microwave background (Bennett et al., 1996a; Net-

terfield et al., 1997; Gunderson et al., 1995; Scott et al., 1995) have been widely interpreted as the result of potential, temperature or velocity fluctuations at the surface of last scattering, originating at very high red shifts ($z > 1000$). However, in many cosmological models, a significant portion of the anisotropies are produced much more recently. In critical density cosmologies, nonlinear gravitational clustering

¹E-mail: sboughn@selene.astro.haverford.edu²E-mail: crittend@cita.utoronto.ca³E-mail: n.g.turok@damtp.cam.ac.uk

produces a time dependent gravitational potential, as bound objects turn around and collapse. This gives rise to CMB anisotropies on small angular scales. In cosmologies with less than critical density (e.g. flat universes with a large cosmological constant and open universes), time dependence of the gravitational potential is induced by a change in the expansion law of the universe at late times, even in the linear perturbation regime. This gives rise to CMB fluctuations on larger scales. The nonlinear effect is usually referred to as the Rees-Sciama (RS) effect (Rees & Sciama, 1968), and the linear effect as the integrated Sachs-Wolfe (ISW) effect (Sachs & Wolfe, 1967). An earlier paper by two of us (Crittenden & Turok, 1996) referred to both as the Rees-Sciama effect.

The recently produced CMB fluctuations result from time variations in the gravitational potential and are correlated with the nearby matter density ($z < 4$). Observing such correlations could place a strong constraint on important cosmological parameters, such as the matter density, Ω_m , and the cosmological constant, Ω_Λ . Above all, such correlations would offer a rare opportunity to observe CMB anisotropies as they are being produced (Crittenden & Turok, 1996).

Implementing this, however, requires a probe of the matter density at high red shifts. Possible probes include radio galaxies and quasars, and a number of large scale surveys of these objects are currently underway. In this paper, a map of the hard X-ray background is used as a measure of the local matter density. X-rays with energies of order a few keV appear to be produced primarily by active galactic nuclei (AGN) (Comastri et al., 1995) and so should reflect the mass distribution on large scales. Here, we investigate the cosmological limits which result from cross correlating the HEAO1 A2 2–10 keV X-ray map (Boldt, 1987) with the four year COBE DMR map of the cosmic microwave background (Bennett et al., 1996a).

2. X-ray emission as a tracer of mass

In order to use the X-ray background in the type

of analysis suggested above two questions must be answered: “How well do X-ray sources trace matter?” and “What is the redshift distribution of the X-ray emission?”. The latter of these questions will be addressed using a particular model of X-ray sources (Comastri et al., 1995) to compute the intensity-redshift distribution, $du(z)/dz$, i.e. the portion of the intensity of the X-ray background that arises at redshift z . The results presented in this paper are not very sensitive to the particular form of $du(z)/dz$ as long as a significant portion of the intensity arises from redshifts of order unity. This is the case for most current models of the X-ray background. How well X-rays trace matter is less well known. In this paper we will assume a simple linear bias, i.e. that the fractional fluctuations in X-ray emissivity are linearly proportional to the fractional mass density fluctuations, $(\delta\epsilon_x/\epsilon_x) = b_x(\delta\rho_m/\rho_m)$, where b_x is the bias factor. The linear bias assumption would hold if the X-ray sources were produced at the high peaks of a Gaussian random field, in which case the bias b_x would be approximately the height ν of the peaks, in units of the standard deviation on the appropriate smoothing scale. More generally, it is quite plausible that X-ray sources trace the matter density, and the linear bias model may be taken as a crude parametrization of this. For example, if X-ray sources are produced by local physical processes which are completely independent of the long wavelength density perturbations, their bias would be unity, since they would merely be test particles clustering as the matter clusters.

While the source of the X-ray background is still very much an area of intense research, it is already clear that discrete sources are the major component. Deep ROSAT observations have resolved $\geq 60\%$ of the soft (0.5–2.0 keV) X-ray background into discrete sources (Hasinger et al., 1993) and the unified AGN (Seyfert galaxies and quasars) models have successfully described both the spectrum and the brightness of the hard (2–10 keV) background (Comastri et al., 1995; Madau et al., 1994; Zdziarski et al., 1993) as well as the local volume emissivity (Miyaji et al., 1994). Despite the successes of these

models, it is quite possible that they will have to be modified in some way (e.g. more detailed evolution, refined spectra, a less ‘unified’ AGN model, a new population of sources, etc.) as more is learned about X-ray sources. In particular, correlation and fluctuation analyses are still not well understood in either the hard or soft bands (Miyaji et al., 1994; Chen et al., 1994; Carrera et al., 1993). However, it seems unlikely that the average flux distribution, $du(z)/dz$, will be greatly changed by such modifications. Given that the ISW effect is not particularly sensitive to the detailed shape of $du(z)/dz$, we do not believe that such modifications to the model will have a large effect on the results of this paper.

The extent to which the X-rays trace the matter distribution is still uncertain. From the dipole anisotropy of the local AGN distribution, Miyaji (1994) estimated that $b_x \Omega_m^{-0.6} \approx 3.5/f$ where f is fraction of the total gravitational acceleration of the Local Group contributed by matter within $45 h^{-1}$ Mpc, Ω_m is the matter density, and h is the Hubble constant in units of $100 \text{ km s}^{-1} \text{ Mpc}^{-1}$. For example, if $\Omega_m = 0.3$ and $f \sim 0.5$, this implies $b_x \approx 3$. However, it is not clear if the bias measured in such nearby X-ray sources is appropriate on the much larger scales of interest for the ISW effect. For example, it is possible that emission from nearby clusters might make the local bias appear higher.

In the context of a given theory, where the power spectrum of density fluctuations is known and appropriately normalized by the COBE detection of the anisotropies, it is also possible to place an upper limit on the X-ray bias by observing the angular auto-correlation function (ACF) of the X-ray background. One can compare this to that predicted by the theory assuming a linear, scale-independent bias. Unfortunately, the large scale ($> 1^\circ$) angular correlations of the X-ray background have not been accurately measured. From our own measurements of the ACF of the hard background we found that, in the context of cold dark matter (CDM) models with a cosmological constant, $b_x \approx 5.6 \Omega_m^{0.53}$ (see Table 1). This should be considered as an upper limit since the HEAO beam size is large ($3^\circ \times 3^\circ$) and can itself induce correlations even when viewing randomly

placed sources. While limits found in this manner are necessarily model dependent, they do provide important context for assessing the viability of a model.

One might argue by analogy with other populations. Ordinary galaxies have correlation lengths of order $r_o \approx 5 h^{-1} \text{ Mpc}$ (Groth & Peebles, 1977) and are thought to be only mildly biased, $b_g \approx 1$. This might be considered a reasonable lower limit to the X-ray bias. The correlation lengths of radio galaxies (Loan et al., 1997; Sicotte, 1995), QSO’s (Andreani & Cristiani, 1992), and groups of galaxies (Bahcall, 1996) are all on the order of $10\text{--}18 h^{-1} \text{ Mpc}$. If, as seems likely, hard X-ray sources have similar clustering properties to these, then we expect the X-ray bias to be of order $b_x \approx 2\text{--}3$. On the other hand, rich clusters of galaxies are even more strongly correlated (Bahcall, 1996), $r_o \approx 20\text{--}25 h^{-1} \text{ Mpc}$ and if X-ray sources are instead like these it would imply $b_x > 3$. It is well known that the X-ray background is highly correlated with these other objects (Refregier et al., 1997; Soltan et al., 1996, 1997; Miyaji et al., 1994); however, the correlation length is still uncertain. It is clear that the X-ray bias (if indeed linear bias is a good description of the distribution of X-ray sources) is not well known. Therefore, we have chosen to report our results with X-ray bias as an unknown parameter.

Finally, as an independent, qualitative check on how X-rays trace mass we have cross-correlated the HEAO 2–10 keV map with the appropriately smoothed and binned Greenbank 5 GHz radio source counts (Gregory & Condon, 1991). The correlation coefficient of these two maps is significant, $\langle \delta n \delta i \rangle / \delta i_{rms} \delta n_{rms} = 0.2 \pm 0.05$, indicating that they are tracing correlated populations. The Greenbank survey is dominated by moderate redshift ($z \sim 1$) sources (Loan et al., 1997; Sicotte, 1995) which implies (with some assumption about X-ray source evolution) that most of contribution to the cross-correlation, $\langle \delta n \delta i \rangle$, comes from the redshift range $0.1 < z < 1$. This supports the unified AGN models for the X-ray background, which suggest that this redshift interval is the source of roughly 25% of the X-ray background (see Fig. 1). This cross-correlation function can also be expressed as

$$\langle \delta n \delta \iota \rangle \approx \langle \iota_R \rangle + w_{XR} \langle n \rangle \langle \iota_X \rangle \quad (1)$$

where ι_R is the X-ray intensity of the radio sources, ι_X the intensity of other X-ray sources in the field, $\langle n \rangle$ is the average number (≈ 42) of radio sources in a resolution element, and w_{XR} is the cross-correlation coefficient between radio sources and the X-ray sources. Since the numerical value of $\langle \delta n \delta \iota \rangle / \langle \iota \rangle$ is 0.03, either 3% of the X-ray background is due to the 5 GHz radio sources or the correlation coefficient between radio sources and X-ray sources is on the order of $w_{XR} \approx 10^{-3}$. In either case, the implication is that X-ray sources are significantly clustered. The Greenbank radio sources are themselves strongly correlated with correlation lengths of $10\text{--}18 h^{-1} \text{ Mpc}$ (Loan et al., 1997; Sicotte, 1995); when smoothed on the HEAO beam scale the radio source correlation coefficient is $w_{RR} \approx 2 \times 10^{-3}$. These values are comparable to w_{XX} deduced from the X-ray autocorrelation function (see Section 4.1) and suggest that the radio and X-ray sources may have comparable biases. Similar results were found cross-correlating the X-ray background with the FIRST radio survey (Cress et al., 1996). These results cannot be made more quantitative without a detailed analysis of the X-ray/radio source cross-correlation (Boughn, 1998).

3. CMB and X-ray correlations

We will focus here on the two point correlations of the microwave temperature and X-ray intensity, and the related power spectrum of the density fluctuations. The density can be written as

$$\rho(x, t) = \bar{\rho}(t)(1 + \delta(x, t)), \quad (2)$$

where $\bar{\rho}(t)$ is the average matter density at proper time t . The power spectrum is defined as the Fourier transform of the two point correlation function and is given by $\langle \delta_{\mathbf{k}} \delta_{\mathbf{k}'}^* \rangle = P_{\mathbf{k}} \delta(\mathbf{k} - \mathbf{k}')$ where $\delta(x, t_0) = \sum_{\mathbf{k}} \delta_{\mathbf{k}} e^{i\mathbf{k} \cdot \mathbf{x}}$ and t_0 is the present time. (Note that we will use \mathbf{x} and \mathbf{k} to refer to comoving position and wavenumber.)

All sky maps of the X-ray intensity or temperature

fluctuations can be naturally expanded in terms of spherical harmonics. For example, we can write the fluctuation in X-ray intensity as

$$\frac{\delta \iota(\mathbf{n})}{\bar{\iota}} = \sum_{l, m} a_{lm}^X Y_{lm}(\Omega_{\mathbf{n}}), \quad (3)$$

where $\delta \iota(\mathbf{n}) = \iota(\mathbf{n}) - \bar{\iota}$ and \mathbf{n} is the unit direction vector. A similar expression can be written for the temperature anisotropy $\delta T(\mathbf{n})$. The expectation value of the moments defines an angular power spectrum

$$C_l = \langle |a_{lm}|^2 \rangle, \quad (4)$$

which is related to the expectation value of the autocorrelation function by

$$\begin{aligned} C(\theta) &= \left\langle \frac{\delta \iota(\mathbf{n})}{\bar{\iota}} \frac{\delta \iota(\mathbf{n}')}{\bar{\iota}} \right\rangle \\ &= \frac{1}{4\pi} \sum_l (2l+1) C_l P_l(\cos \theta), \end{aligned} \quad (5)$$

where $\cos \theta = \mathbf{n} \cdot \mathbf{n}'$ and $P_l(x)$ is a Legendre polynomial.

3.1. CMB anisotropies

In the approximation of instantaneous recombination, the microwave anisotropy in a direction \mathbf{n} on the sky is given in Newtonian gauge by

$$\frac{\delta T}{T}(\mathbf{n}) = \left[\frac{1}{4} \delta_{\gamma} + \mathbf{v} \cdot \mathbf{n} + \Phi \right]_{\tau_r}^{\tau_0} + 2 \int_{\tau_r}^{\tau_0} d\tau \dot{\Phi}(\tau, \mathbf{n}(\tau_0 - \tau)). \quad (6)$$

The integral is over the conformal time τ , and τ_r and τ_0 are the times of recombination and the present, respectively. The first term ($\frac{1}{4} \delta_{\gamma}$) represents density perturbations of the radiation-baryon fluid, the second term is the Doppler shift ($\mathbf{v} \cdot \mathbf{n}$), and the third is the Newtonian potential (Φ), where all of these are evaluated on the surface of last scattering. The last term, usually called the Integrated Sachs-Wolfe (ISW) term, represents the effect of a time varying gravitational potential along the line of sight. Heuristically, it represents the redshifting of photons

which ‘climb out’ of a different potential than they ‘fell into’.

The CMB anisotropies are the sum of contributions created near the surface of last scattering and those created recently by the ISW effect. Since the two contributions are associated with perturbations of very different wavelengths, they are nearly uncorrelated except on the largest angular scales. The moments can be written as

$$a_{lm}^T = a_{lm}^{\text{ISW}} + a_{lm}^{\text{LS}} \quad (7)$$

and the fact that they are weakly correlated implies

$$C_l^T = C_l^{\text{ISW}} + C_l^{\text{LS}}, \quad (8)$$

where $C_l^{\text{ISW}} = \langle |a_{lm}^{\text{ISW}}|^2 \rangle$ and $C_l^{\text{LS}} = \langle |a_{lm}^{\text{LS}}|^2 \rangle$.

The ISW term arises when the CMB photons pass through a potential fluctuation which is evolving in time, i.e.

$$a_{lm}^{\text{ISW}} = 4\pi i \sum_k \frac{\delta_k}{p_k^{1/2}} \int 2\dot{\Phi}(k,r) j_l(kr) dr Y_{lm}(\Omega_k), \quad (9)$$

where r is the conformal distance, $\tau_0 - \tau$, and $j_l(x)$ is a spherical Bessel function. Squaring this and integrating over the directions of \mathbf{k} , we find

$$C_l^{\text{ISW}} = \frac{2}{\pi} \int k^2 dk \left| \int 2\dot{\Phi}(k,r) j_l(kr) dr \right|^2. \quad (10)$$

3.2. The X-ray model

To evaluate the expected X-ray brightness fluctuations, a model is needed which describes the redshift distribution of the sources, as well as their luminosities. We consider the unified AGN model of Comastri et al. (1995), which reproduces source number counts and the flux and spectrum of the X-ray background in both soft and hard X-ray bands. In this model, AGN are divided into two luminosity classes, Seyfert galaxies and quasars, which range in X-ray luminosity from $10^{42} \text{ erg s}^{-1}$ to $10^{47} \text{ erg s}^{-1}$ (0.3–3.5 keV). The power-law luminosity function has a break at a luminosity of $L_B = 6.9 \times 10^{43} \text{ erg s}^{-1}$ where AGN with luminosities $L < L_B$ are designated Seyferts and those with $L > L_B$ are designated quasars.

The AGN are thought to be surrounded by an absorbing molecular torus, with the amount of absorption depending on the line of sight. As an approximation, the AGN are divided into five absorption classes characterized by their H column density, with column densities ranging from zero up to $N_H = 10^{25} \text{ cm}^{-2}$. The number density of each class is proportional to the number density of unabsorbed AGN, i.e. $n_{s,i} = w_i n_{s,0}$ and $n_{q,i} = w_i n_{q,0}$ where $n_{s,0}$ ($n_{q,0}$) is the total number of unabsorbed Seyferts (quasars) and the index i runs over absorption class. The relative density in each class is assumed to be independent of both source luminosity and redshift. A detailed description of this division and the associated spectra can be found in Comastri et al. (1995).

The average number of AGN in a volume at redshift z is $d\tilde{N}(z) = n(z)dV$ where $dV = d_A^2(z)d\Omega dl$, $d_A(z)$ is the angular diameter distance, $d\Omega$ is the solid angle and dl is proper radial distance. Proper distance can be expressed as

$$dl = dt = \frac{da}{a'} = \frac{dz}{1+z} \frac{a}{a'}, \quad (11)$$

where “ a ” is the expansion factor and primes indicate derivatives with respect to proper time. In the Comastri model, the comoving number density is assumed to be constant, so that $n(z) = n_0(1+z)^3$ where n_0 is the total unabsorbed AGN density. It can be expressed as

$$n_0 = n_{s,0} + n_{q,0} = \int_{L_{\min}}^{L_B} \phi_s(L) dL + \int_{L_B}^{L_{\max}} \phi_q(L) dL,$$

where ϕ_s is the luminosity function of Seyferts and ϕ_q the luminosity function of quasars.

Another key feature of most X-ray models is that the X-ray luminosity evolves with redshift as

$$L(z) = L(0) \times (1+z)^\beta. \quad (12)$$

The Comastri model assumes $\beta = 2.6$ and a cutoff redshift, $z_{\text{cutoff}} = 2.25$, above which the luminosity is assumed to be constant, up to maximum redshift of

$z_{\max} = 4$. There is some evidence the evolution could be even stronger than assumed by Comastri et al., with a slightly higher index, $\beta \approx 3$, and a somewhat lower cutoff redshift, $z_{\text{cutoff}} \approx 1.8$. A detailed examination of these luminosity models is found in Boyle et al. (1994).

The flux received from an object at a given redshift is related to its luminosity by

$$\mathcal{F}(z, L) = \frac{L(z)}{4\pi d_L^2} \quad (13)$$

where the luminosity distance d_L is related to the angular distance by $d_L = d_A(1+z)^2$. For band limited detectors this relation becomes

$$\mathcal{F}(z, L, I) = \frac{f(z, I)L(z)}{4\pi d_L^2}. \quad (14)$$

where $L(z)$ now represents the energy emitted in the detector band $[E_1, E_2]$ and $f(z, I)$ is the usual K-correction

$$\begin{aligned} f(z, I) &= \frac{L_{\text{detected}}}{L} = \frac{\int_{E_1(1+z)}^{E_2(1+z)} I(E) dE}{\int_{E_1}^{E_2} I(E) dE} \\ &= \frac{(1+z) \int_{E_1}^{E_2} I(E(1+z)) dE}{\int_{E_1}^{E_2} I(E) dE}. \end{aligned} \quad (15)$$

Since the K-correction depends on $I(E)$, the spectrum of the source, it is a different function for each absorption class.

At a given redshift the flux averaged over the various types of AGN is obtained by summing over both luminosity and absorption, i.e.,

$$\begin{aligned} \mathcal{F}(z) &= \frac{\int_{L_{\min}}^{L_B} \phi_s(L) dL \sum w_i \mathcal{F}(z, L, I_{Si})}{\int_0^{\infty} \phi(L) dL \sum w_i} \\ &\quad + \frac{\int_{L_B}^{L_{\max}} \phi_q(L) dL \sum w_i \mathcal{F}(z, L, I_{Qi})}{\int_0^{\infty} \phi(L) dL \sum w_i} \\ &= \frac{(1+z)^\beta}{4\pi d_L^2} \left(\langle L_S \rangle \sum_i w_i f(z, I_{Si}) \right. \\ &\quad \left. + \langle L_Q \rangle \sum_i w_i f(z, I_{Qi}) \right) \end{aligned} \quad (16)$$

where

$$\langle L_S \rangle = \frac{\int_{L_{\min}}^{L_B} \phi_s(L) L dL}{n_0 \sum w_i}$$

and

$$\langle L_Q \rangle = \frac{\int_{L_B}^{L_{\max}} \phi_q(L) L dL}{n_0 \sum w_i}.$$

We denote the term in parentheses as $L_K(z)$, the average K-corrected luminosity per unit volume. For the absorbed spectra used by Comastri et al. (1995), this factor can be approximated by $L_K(z) \propto (1+z)/(1+0.15z)$.

Finally, the “space weighting function”, i.e. the contribution to the band limited X-ray intensity as a function of redshift, is

$$\frac{d\bar{N}(z)}{dz} \mathcal{F}(z) = n_0 (1+z)^3 d_A^2 d\Omega \frac{1}{1+z} \frac{a}{a'} \frac{(1+z)^\beta}{4\pi d_L^2} L_K(z). \quad (17)$$

Using the fact that $a'/a = H_0(\Omega_A + \Omega_m(1+z)^3)^{1/2}$ for the flat cosmologies studied here, and simplifying, the weighting function is

$$\frac{d\bar{N}(z)}{dz} \mathcal{F}(z) = \frac{n_0(1+z)^{\beta-2} L_K(z) d\Omega}{4\pi H_0(\Omega_A + \Omega_m(1+z)^3)^{1/2}}. \quad (18)$$

Fig. 1 is a plot of $d\bar{N}(z)/dz \mathcal{F}(z)$ in arbitrary units. It is clear from this figure that much of the flux arises from sources at redshifts of order $z \approx 1-2$ as required in order to detect a significant ISW effect. The shape of the distribution is fairly flat and is similar to (though it extends to somewhat higher redshifts) the distribution used in Crittenden & Turok (1996) which used $d\bar{N}(z)/dz$ measured in a flux limited survey and assumed that the flux received from an object at a given redshift was constant.

It should be noted that for their analysis Comastri et al. (1995) adopted a Hubble constant of $H_0 = 50 \text{ km s}^{-1} \text{ Mpc}^{-1}$ and a deceleration parameter of $q_0 = 0$. The fact that these differ from the cosmological parameters of the models in this paper is not of great concern since ultimately we only use the space weighting function which is directly tied to observations and is, therefore, relatively insensitive to the cosmological model. In any case, as was pointed out

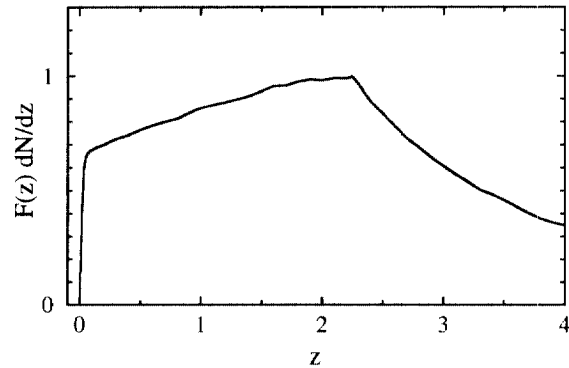


Fig. 1. The redshift distribution of contributions to the intensity fluctuations in the cosmic X-ray background, based on the model of Comastri, et al. The cutoff at low redshift results from excluding high flux X-ray sources, while the cusp at $z = 2.25$ results from the change in the luminosity evolution of the sources.

previously, the ISW effect is not overly sensitive to the space weighting function.

3.3. X-ray correlations

Given a model for the space weighting function, we then must calculate the fluctuations in intensity. Let $N(\mathbf{x}, z)$ be the number of AGN in a volume dV at a position \mathbf{x} and redshift z . If number density fluctuations are assumed to be related to mass density fluctuations by a redshift dependent bias b_x , then

$$\begin{aligned} \frac{\delta N(\mathbf{x}, z)}{\bar{N}(z)} &= \frac{\delta n(\mathbf{x}, z)}{\bar{n}(z)} \equiv b_x(z) \frac{\delta \rho(\mathbf{x}, z)}{\bar{\rho}(z)} \\ &= b_x(z) \delta(\mathbf{x}, z), \end{aligned} \quad (19)$$

where $\bar{N}(z)$ is the average number of AGN, and

$$N(\mathbf{x}, z) = \bar{N}(z) (1 + b_x(z) \delta(\mathbf{x}, z)). \quad (20)$$

For simplicity, throughout we will assume that the bias is independent of redshift.

The evolution of the mass density fluctuation is characterized by $\delta(\mathbf{x}, z) = \delta(\mathbf{x}, 0) D(z)$. For flat, matter dominated cosmologies, perturbations grow proportionally to the scale factor, that is, $D(z) = (1+z)^{-1}$. However, for alternative cosmologies such as those with a cosmological constant, or with significant curvature, perturbations eventually cease to grow.

The intensity of X-rays in a given direction is just the sum of the flux from each galaxy,

$$I(\mathbf{n}) = \int dN(\mathbf{x}, z) \mathcal{F}(z) \quad (21)$$

where $\mathcal{F}(z)$ is the flux we receive from a galaxy at redshift z and $\mathbf{n} = \mathbf{x}$. Thus, the X-ray intensity fluctuations on the sky are

$$\frac{\delta I(\mathbf{n})}{\bar{I}} = \frac{\int \mathcal{F}(z) \frac{d\bar{N}}{dz} b_x(z) D(z) \delta(\mathbf{x}, 0) dz}{\int \mathcal{F} d\bar{N}}. \quad (22)$$

This allows one to solve for the X-ray correlation

function. By Fourier expanding the present density fluctuation,

$$\begin{aligned}\delta(\mathbf{x}, 0) &= \sum_{\mathbf{k}} \delta_{\mathbf{k}} e^{i\mathbf{k} \cdot \mathbf{x}} \\ &= \sum_{\mathbf{k}} \delta_{\mathbf{k}} 4\pi \sum_{m,l} i^l j_l(kr) Y_{lm}(\Omega_{\mathbf{n}}) Y_{lm}^*(\Omega_{\mathbf{k}}).\end{aligned}\quad (23)$$

Inserting this into Eq. (22), one can show that

$$\begin{aligned}a_{lm}^x &= \frac{4\pi i^l \int \mathcal{F}(z) \frac{d\bar{N}}{dz} b_x(z) D(z) \sum_{\mathbf{k}} \delta_{\mathbf{k}} Y_{lm}^*(\Omega_{\mathbf{k}}) j_l(kr) dz}{\int \mathcal{F} d\bar{N}} \\ &= 4\pi i^l \sum_{\mathbf{k}} \delta_{\mathbf{k}} f_l(k) Y_{lm}^*(\Omega_{\mathbf{k}})\end{aligned}\quad (24)$$

where

$$f_l(k) = \frac{\int \mathcal{F}(z) \frac{d\bar{N}}{dz} b_x(z) D(z) j_l(kr) dz}{\int \mathcal{F} d\bar{N}}.\quad (25)$$

The argument defines a weighting function which determines how deeply in redshift the X-rays probe. As above, using the expression for the moments and integrating over the directions of \mathbf{k} , the X-ray angular power spectrum is

$$C_l^x = \frac{2}{\pi} \int k^2 dk P_k f_l^2(k).\quad (26)$$

If the fluctuations have a Harrison-Zeldovich-Peebles spectrum, $P_k \propto k$, then this implies that C_l^x is constant for low multipoles. The X-ray autocorrelation function is given by (see Eq. (5))

$$C_x(\theta) = \frac{1}{4\pi} \sum_l (2l+1) C_l^x P_l(\cos\theta).\quad (27)$$

Note that $C_x(\theta)$ is proportional to b_x^2 . This treatment is similar to previous calculations of the X-ray background fluctuations (Carrera et al., 1997; Lahav et al., 1997).

In addition to fluctuations from structure, Poisson fluctuations due to the discreteness of the X-ray sources will also contribute to the X-ray auto-correlation function. In general, the random placement of

nearby objects causes this term to dominate the correlation function and the contribution formally diverges if arbitrarily high flux objects are considered. In practice, a high end flux cutoff eliminates the divergence. The Poisson contribution to the correlation can be written as

$$\langle \delta u(\mathbf{x}) \delta u(0) \rangle_{\text{Poisson}} = \int d^3x' \bar{n}(z') W(\hat{n}, \hat{n}') W(0, \hat{n}') \mathcal{F}^2(z')\quad (28)$$

where $W(\hat{n}, \hat{n}')$ represents the angular beam profile of the detector. This contribution to the ACF, which is independent of bias, must be corrected for in order to compare observations with cosmological models.

3.4. Cosmological models and the power spectrum

The models we consider are spatially flat and are primarily composed of cold dark matter (CDM) with a cosmological constant. We assume the baryon density is constrained by $\Omega_b h^2 = 0.0125$, though the dependence on baryon density is relatively weak. The initial fluctuations are assumed to be adiabatic fluctuations with a scale invariant Harrison-Zeldovich-Peebles spectrum. The present power spectrum is determined from the transfer function and to simplify the analysis, we have focused on models which have transfer functions with the same shape, as parameterized by $\Gamma = \Omega_m h e^{-(\Omega_b + \Omega_b' / \Omega_m)} = 0.25$. (See, for example, Efstathiou (1996) and references therein.)

We normalize the models using the variance in the CMB on 10° , as measured by COBE DMR (Banday et al., 1997). From the growth of perturbations, the power spectrum scales approximately as $\Omega_m^{-1.54}$ (Efstathiou et al., 1992). However, at large Ω_A , this dependence is softened due to the late time ISW effect. While a more complete analysis of the model normalization can be made using the full COBE data (Sugiyama, 1995; Gorski et al., 1995; White & Bunn, 1995; Bunn & White, 1997), using the 10° variance is adequate for the present treatment. This normalization differs from previous calculations of the X-ray fluctuations which normalized with respect

to σ_8 , the standard deviation of the mass in a sphere of radius $8 h^{-1} \text{ Mpc}$ (Carrera et al., 1997). Roughly, the COBE normalization corresponds to a normalization of $\sigma_8 = 0.7 \Omega_m^{-0.6}$ for the $\Gamma = 0.25$ models we consider here.

Since we are interested in the X-ray bias, it is important to understand what part of the power spectrum is probed by the fluctuations in the X-ray background. A rough estimate can be made from the flux cut of the survey and its angular resolution. For the given flux cut, $1 \times 10^{-11} \text{ erg cm}^{-2} \text{ s}^{-1}$, an AGN with mean luminosity $L \approx 7 \times 10^{43} h^2 \text{ erg s}^{-1}$ would be removed from consideration if it were closer than $120 h^{-1} \text{ Mpc}$, corresponding to a redshift of $z = 0.04$. Obviously, objects dimmer or brighter than the mean luminosity could be closer or further away, but this distance should be a reasonable approximation. Given a resolution of approximately 3° , this implies that the correlation is sensitive to structures on scales greater than $6 h^{-1} \text{ Mpc}$ or so.

For a given theoretical model, this can be made more rigorous by considering which wavenumbers contribute to the correlation. Assuming a Gaussian window function, the smoothed correlation function can be written as

$$C_X(\theta) = \frac{1}{4\pi} \sum_l (2l+1) C_l^X P_l(\cos\theta) \times \exp\left(-\frac{\ell(\ell+1)\theta_B^2}{8\log 2}\right), \quad (29)$$

where θ_B denotes the FWHM (full width half max) resolution. From the above expression for C_l , we can define

$$W^2(\theta_B, k) = \frac{1}{2\pi^2} \sum_l (2l+1) P_l f_l^2(k) \times \exp\left(-\frac{\ell(\ell+1)\theta_B^2}{8\log 2}\right), \quad (30)$$

(This is analogous to W_T^2 defined by Bond & Efstathiou (1987).) With this, $k^3 W^2(\theta_B, k)$ then represents the contribution to the X-ray variance for a given resolution from each log interval of wavenumber.

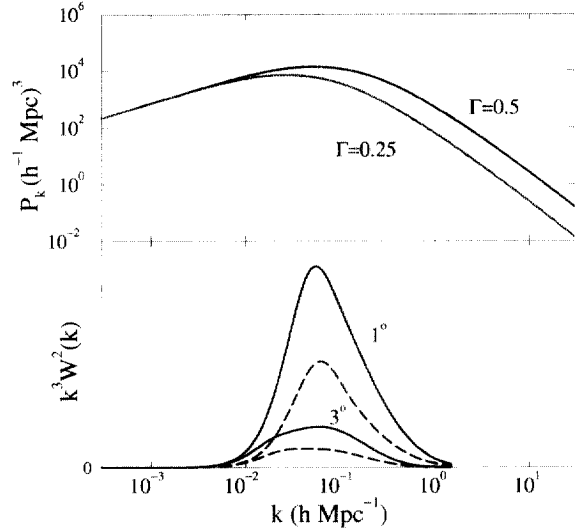


Fig. 2. The top figure shows the power spectrum for density fluctuations for two different values of Γ . The figure below shows where the zero lag X-ray correlation arises as a function of wavenumber for different resolutions. The X-ray variance, $(\delta X/X)^2$, is proportional to the area underneath the curves. Dashed lines represent an $h = 0.32$, $\Omega_m = 1$ model, while the solid lines $h = 0.56$, $\Omega_m = 0.5$ model.

Fig. 2 shows the contributions versus wavenumber for two sample models. One can see that the correlations arise due to modes between 0.01 – $0.5 h \text{ Mpc}^{-1}$, near the peak of the power spectrum. Thus it spans the gap between those sampled in large scale structure surveys and those probed by CMB measurements. There are two primary effects which determine the inferred X-ray bias: the normalization of the spectrum and the evolution of perturbations, and these effects partially offset each other. The X-ray bias scales as $\Omega_m^{0.53}$ and σ_8^2 , the area under the curve, scales as $\Omega_m^{-1.06}$.

3.5. Predictions for the cross correlation

Only the anisotropies created recently are correlated with the X-ray fluctuations described above. Since that is the case, anisotropies produced at last scattering can be ignored and only the ISW contribu-

tion to the cross correlation need be considered. The cross correlation between the X-ray and the microwave backgrounds is defined as

$$C^{XT}(\theta) = \left\langle \frac{\delta u(\mathbf{n})}{\bar{u}} \frac{\delta T(\mathbf{n}')}{T} \right\rangle$$

$$= \frac{1}{4\pi} \sum_l (2l+1) C_l^{XT} P_l(\cos\theta). \quad (31)$$

Following the same procedures used above, these coefficients can be shown to be

$$C_l^{XT} = \langle a_{lm}^X a_{lm}^{ISW*} \rangle$$

$$= \frac{2}{\pi} \int k^2 dk f_l(k) P_k^{1/2} \int 2\Phi(k,r) j_l(kr) dr. \quad (32)$$

Because of the statistical nature of the background anisotropies, the correlations expressed in Eq. (32) represent ensemble averages. A particular realization, $C_{\text{real}}(\theta)$, of $C(\theta)$ can be easily evaluated. Assuming each a_{lm} is gaussian distributed with variance C_l , then

$$a_{lm}^T = \sqrt{C_l^T} \xi_{1,m}$$

$$a_{lm}^X = \frac{C_l^{XT}}{\sqrt{C_l^T}} \xi_{1,m} + \left(C_l^X - \frac{[C_l^{XT}]^2}{C_l^T} \right)^{1/2} \xi_{2,m} \quad (33)$$

where $\xi_{i,m}$ are numbers randomly chosen from independent gaussian distributions with $\sigma = 1$. A particular realization is, then,

$$C_{\text{real}}^{XT}(\theta) = \frac{1}{4\pi} \sum_l (2l+1) R_l^{XT} P_l(\cos\theta) \quad (34)$$

where $R_l^{XT} = \sum_m a_{lm}^T a_{lm}^X / (2l+1)$. The distributions of $C_{\text{real}}^{XT}(0)$ for 1000 realizations of several different cosmological constant models are represented in Fig. 3.

The spreads of the distributions reflect chance alignments of regions of enhanced (depleted) X-ray intensity with regions of enhanced (depleted) CMB intensity. The latter are due primarily to the CMB anisotropies produced at last scattering and are, therefore, uncorrelated with X-ray emission. These accidental correlations can be thought of as a form of “cosmic variance”. The curves in Fig. 3 were

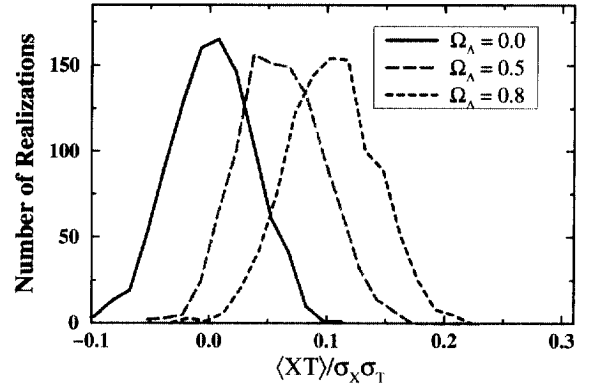


Fig. 3. Distribution of $\langle XT(0) \rangle$ for 1000 realizations with different values of Ω_Λ .

computed assuming full sky maps. Limited sky coverage increases the spread. It should be noted that widths of the distributions are approximately independent of Λ . The effect of the usual cosmic variance, i.e. the variance of the actual ISW effect due to the statistical nature of density fluctuations, is small. The profiles are roughly Gaussian and we treat this effect as any other source of noise in the measurement.

Note that we have chosen to plot the quantity $C^{XT}(\theta)/\sigma_X\sigma_T$ which is independent of the bias b_x in the theoretical calculations. All of the quantities in this expression are measurable. $\sigma_T^2 \equiv C^T(0)$ has been measured by COBE and a limit on $C^{XT}(\theta)$ is reported in this paper. However, as discussed above, the measurements of $\sigma_X^2 \equiv C^X(0)$ are still ambiguous. In order to compare the model predictions in Fig. 3 with observations, we will take $C^X(0)$ to be that predicted by a given cosmological model modulo b_x^2 . The results will then be given as a limit on the cosmological constant in terms of the unknown X-ray bias.

4. The HEAO1-A2 and COBE maps

The HEAO1 A2 experiment was designed to measure surface brightness in the 0.1–60 keV X-ray band (Boldt, 1987). The present analysis is from two

medium energy detectors (MED) with different fields of view ($3^\circ \times 1.5^\circ$ and $3^\circ \times 3^\circ$ FWHM) and two high energy detectors (HED3) with the same fields of view. Counts from these four detectors were combined and binned in 24,576 $1.3^\circ \times 1.3^\circ$ pixels in an equatorial quadrilateralized spherical cube projection on the sky (White & Stemwedel, 1992). The combined map has an effective angular resolution diameter (FWHM) of 3.3° and a spectral resolution of roughly 2–10 keV (Jahoda & Mushotzky, 1989). All data used in this analysis were collected during the 6-month period beginning on day 322 of 1977.

The dominant feature in the HEAO map is the Galaxy, so all data within 20° of the Galactic plane and within 30° of the Galactic center were cut from the map. In addition, 10° diameter regions around 90 discrete X-ray sources with 2–10 keV fluxes larger than $3 \times 10^{-11} \text{ erg s}^{-1} \text{ cm}^{-2}$ (Piccinotti et al., 1982) were removed. Finally, the X-ray map itself was searched for weak point “sources” that exceeded the nearby background by a specified amount and 7° diameter regions around these were removed. Cuts were made at several levels from 4 to 10 times the photon counting noise resulting in “cleaned” maps with sky coverage of from 26% to 47%. The analysis that follows is for the 6σ cut which removed sources with fluxes greater than $1 \times 10^{-11} \text{ erg s}^{-1} \text{ cm}^{-2}$. The final “cleaned” map corresponds to 1/3 of full sky coverage; however, the results of this paper are largely independent of the level of the cuts.

Even after cleaning, the HEAO map has several components of large-scale systematic structure which can be corrected for. If the dipole moment of the CMB is a kinematic effect, as it has been widely interpreted (Bennett et al., 1996a), then the hard X-ray background should possess a similar dipole structure (Compton-Getting effect) with an amplitude of $\delta\epsilon/\epsilon = 4.3 \times 10^{-3}$. The cleaned map was corrected for this effect. In addition, a linear time drift in detector sensitivity (Jahoda, 1993) results in large-scale structure of known form. Finally, the 2–10 keV background shows evidence of high latitude Galactic emission as well as emission associated with the Supergalactic plane (Jahoda, 1993). We

modeled these latter three effects as a combination of a linear time drift, a Galactic secant law, the Haslam 408 MHz Galactic radio map, and a simple pancake Supercluster. This model was linearly regressed to the cleaned data and subsequently subtracted from the map. Of the four parameters, the time drift and secant law were most significant. Correcting for these effects significantly reduced the large scale structure in the X-ray autocorrelation function but had little effect at small angular scales as expected (see Section 4.1). When the Compton-Getting dipole was included in the fit (3 additional parameters), the results did not change significantly.

Because of the ecliptic longitude scan pattern of the HEAO satellite, sky coverage and, therefore, photon shot noise were not uniform. However, the mean variance of the cleaned, corrected map, 1.63×10^{-2} TOT counts/sec, is considerably larger than the mean variance of photon shot noise, 0.67×10^{-2} TOT counts/sec, where TOT counts/sec is the standard HEAO1 A2 normalization for the 2–10 keV band (Allen et al., 1994). The correlation analysis of Section 4.1 demonstrates that the variance in the HEAO map is due to small angular scale ($\leq 5^\circ$) intensity fluctuations; therefore, the X-ray map is dominated by “real” (not photon noise) structure. For this reason, in the correlation analyses that follow, we chose to weight each pixel equally.

The CMB map was constructed from the 53 GHz and 90 GHz 4-year COBE DMR maps as obtained from the National Space Science Data Center (Bennett et al., 1996b). Each map consists of 6144 $2.6^\circ \times 2.6^\circ$ pixels in an ecliptic quadrilateralized spherical cube projection, i.e. half the resolution of the X-ray map. The 31 GHz maps have considerably larger instrument noise and Galactic contamination and were not used in this analysis (Bennett et al., 1996a). These four temperature maps (A and B channels for each frequency) were converted from antenna to thermodynamic temperature and then combined in a straight average to form the composite CMB map. This straight average map has somewhat larger instrumental noise than a noise weighted average map; however, the noise in the crosscorrelation function is dominated by “cosmic variance” (see

Section 4.1) and we felt that a straight average would be more likely to minimized unknown systematic effects in the composite map. The same Galactic cut (within 20° of the Galactic plane and within 30° of the Galactic center) was applied to the CMB map as to the X-ray map which results in 64% sky coverage.

The only correction made to the cleaned composite CMB map was to fit and remove the dipole moment. Since the quadrupole moment was included in the analysis of section II-C, no attempt was made to remove it from the data. The removal of a secant law fit to high Galactic latitude emission made no significant difference in the cross-correlation function (see Section 4.1) and so the CMB map was not corrected for Galaxy emission. In any case, the analysis of this paper concerns the shape of the cross-correlation function at relatively small angular scales ($\leq 20^\circ$) and is not overly sensitive to the presence of large scale structure in the map.

As with HEAO, the COBE satellite sky coverage was not uniform; therefore, instrument noise per pixel is also not uniform over the sky. In this case the mean variance in the cleaned, corrected CMB map is $5.0 \times 10^{-3} \text{ mK}^2$ whereas the mean variance of instrument noise is $4.1 \times 10^{-3} \text{ mK}^2$, i.e. at the resolution of the map, instrument noise dominates real structure. However, when smoothed in 10° bins, instrument noise variance becomes $3.4 \times 10^{-4} \text{ mK}^2$ compared to the $9.0 \times 10^{-4} \text{ mK}^2$ fluctuations of the CMB (Banday et al., 1996). Therefore, in the correlation analyses that follow, we also chose to weight each CMB pixel equally.

4.1. The X-ray auto-correlation function

The intensity auto-correlation (ACF) is calculated using,

$$\langle XX(\theta) \rangle = \frac{\sum_{i,j} (I_i - \bar{I})(I_j - \bar{I})}{N_\theta}, \quad (35)$$

where the sum is over pairs of pixels separated by θ and N_θ is the number of such pairs. Note that the pairs are given equal weight as discussed above.

The results for the cleaned X-ray map are shown

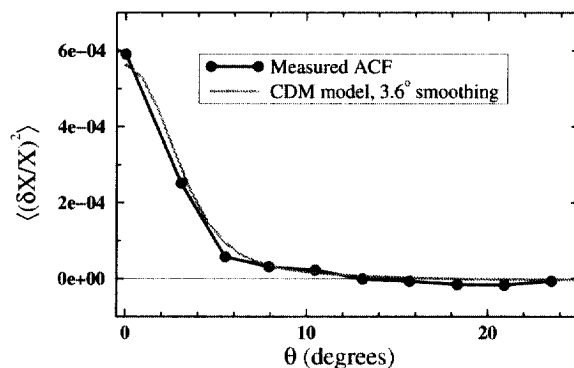


Fig. 4. The auto-correlation function for the HEAO1-A1 X-ray map, normalized in terms of the mean intensity. Shown for comparison is the theoretical prediction for a COBE normalized CDM model with an effective smoothing of 3.6° FWHM.

in Fig. 4. The value at $\theta = 0$ has been corrected for contribution of uncorrelated photon shot noise. To check for the contribution to the ACF of weak X-ray sources in nearby galaxies, 4° diameter holes around all (2367) galaxies in the Tully Atlas of Nearby Galaxies (Tully, 1988) were cut from the map. These cuts did not significantly change the ACF.

Taking into account the finite angular resolution of the HEAO map, the amplitude of the ACF is somewhat smaller than that found by Soltan et al. (1996) for the ROSAT 0.5–2 keV. However, it should be noted that the Soltan et al. results are inconsistent with other measurements (Chen et al., 1994; Carrera et al., 1993) leading them to hypothesize diffuse emission from large (20 Mpc) clouds of gas.

It should be emphasized that the ACF in Fig. 4 has not been corrected for Poisson noise due to unresolved sources. We have calculated the Poisson contribution (Eq. (27)) for the model of Comastri et al. (1995) and found that, for these sources, it is substantially less than the measured value. However, there could be contributions from other types of sources not accounted for in this model. The source counts of Piccinotti et al. (1982) and Butcher (see Carrera et al., 1993) imply there may be a substantial amount of source confusion. Carrera et al. (1993), using data from the *Ginga* satellite, find a signal

consistent with pure Poisson noise. Our observations, however, are within their upper limits. Adding to the confusion, the poor angular resolution of HEAO results in shape of the ACF being dominated by the beam profile. For these reasons we have not chosen to estimate the correction for source confusion and the data in Fig. 4 should be considered an upper limit to the ACF due to clustering of X-ray sources.

Fig. 4 also shows the theoretical ACF arising from a CDM power spectrum with $\Lambda = 0.5$, ($\Gamma = 0.25$), a bias of $b_x = 3.9$, and smoothed by a 3.6° gaussian beam. Recall that the height of the theoretical ACF is proportional to b_x^2 . The sources were assumed to be distributed as in the model of Comastri et al. (1995) with a flux cutoff equal to that applied to the real data. Clearly this bias is a good fit to the model; however, to the extent that the observed ACF is contaminated by source confusion, it should be considered an upper limit for this model. Raising Γ has the effect of adding small scale power, and so would reduce the bias required to fit the X-ray ACF.

4.2. The HEAO/COBE cross correlation

The cleaned, corrected X-ray map was reprojected onto the sky to match the COBE map, i.e., an ecliptic quadrilateralized spherical cube projection with $2.6^\circ \times 2.6^\circ$ pixels. Let w_i be the number of original pixels combined to form one pixel in the new projection. The value of w_i for most pixels was 4; however, because of the transformation to ecliptic coordinates, w_i ranged from 1 to 6. The terms in the cross-correlation function (CCF) are weighted with these values. The cross correlation is then computed as

$$\langle TX(\theta) \rangle = \frac{\sum_{\theta_{ij}=\theta} X_i w_i T_j}{\sum_{\theta_{ij}=\theta} w_i}, \quad (36)$$

where the sum is over all pairs with angular separation θ .

The resulting cross correlation is shown in Fig. 5, where the normalization is with respect to the

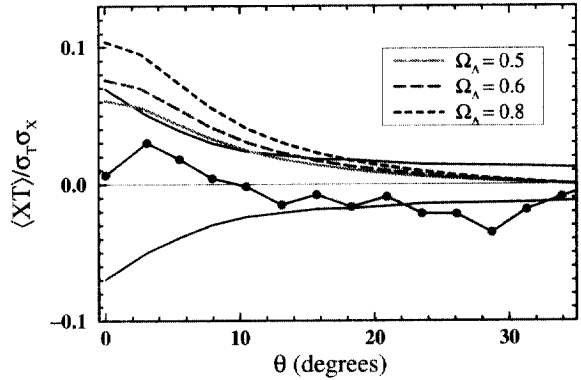


Fig. 5. The cross correlation between the four year COBE map and the HEAO1-A2 X-ray map, normalized by the rms fluctuation of each map. Also shown are the expected correlations for a range of values for the cosmological constant. (The standard CDM model predicts no correlation.) The bold lines show the rms correlations resulting from noise and cosmic variance.

measured rms fluctuations of the two maps. Also shown are the theoretical predictions for cosmological constant models with varying Λ . As described previously, the Hubble constant has also been varied to keep the shape parameter, Γ , fixed. Finally, the solid curves represent the 1σ uncertainty due to the combination of cosmic variance, instrument noise, and photon shot noise. The spread in the distribution illustrated in Fig. 3 did not include the effects of map cleaning, map correction, and reduced sky coverage. In addition, there are quite likely additional fluctuations in the X-ray map that do not appear the X-ray model, e.g. relatively nearby clusters of galaxies. Therefore, we chose to compute the total “noise” by a Monte Carlo method wherein the real, cleaned X-ray map was cross-correlated with an ensemble of 400 randomly generated CMB maps. These latter maps consisted of random realizations of instrument noise and cosmic structure which was constructed so as to have the same ACF profile as the actual COBE data. All the Monte Carlo CMB maps were cleaned (Galaxy cut) and corrected (dipole removal) with the same procedure as used on the real map. The resultant total noise is correlated on angular scales of about 10° . This is due primarily to the finite angular resolution of the COBE map. It is clear from Fig. 5

that the data are consistent with the hypothesis that the two maps are uncorrelated.

The above results assume that fluctuations in the X-ray map are not dominated by Poisson fluctuations of unresolved sources. If there is a significant contribution to the X-rays from this Poisson noise, then both the inferred X-ray bias and the predictions for the theoretical correlation are reduced by a factor of $\sigma_{\text{Structure}}/(\sigma_{\text{Structure}}^2 + \sigma_{\text{Poisson}}^2)^{1/2}$. Therefore, for any particular bias, the model amplitudes should be scaled as $b_x/5.6 \Omega_m^{0.53}$. In any case, it seems unlikely that the bias would be less than unity.

The upper limit of the CCF at $\theta = 0$ is consistent with previous correlation analyses (Boughn & Jahoda, 1993; Banday et al., 1996) between HEAO1-A2 and temperature anisotropy maps. The correlation analysis of the COBE DMR maps and the ROSAT PSPC All-Sky Survey (Kneissl et al., 1997) shows somewhat more structure than Fig. 4. This is presumably due to a larger Galactic contribution at 1 keV.

5. Discussion

As previously discussed, the observed HEAO/COBE cross-correlation is consistent with there being no underlying ISW effect, i.e. no cosmological constant. Since the effective errors computed by Monte Carlo analysis (see Section 4.2) are consistent with being derived from a correlated gaussian distribution, we can quantify this by performing a maximum likelihood analysis. The likelihood is defined by

$$\mathcal{L} = (2\pi)^{-N/2} [\det R_{ij}]^{-1/2} \times \exp[-\frac{1}{2} R_{ij}^{-1} (y_i - \bar{y}_i)(y_j - \bar{y}_j)], \quad (37)$$

where R_{ij} is the covariance matrix and \bar{y}_i is the theoretical prediction for the i^{th} observation. To a good approximation, the theoretical cross-correlation curves in Fig. 5 have the same shape and only differ in amplitude (which depends only on Ω_A).

$$\langle TX(\theta) \rangle = A(A)f(\theta) \quad (38)$$

where $f(0^\circ) = 1$. Maximizing the likelihood for this amplitude, one finds

$$A = \frac{\sum_{ij} R_{ij}^{-1} (f_i y_j + f_j y_i)}{2 \sum_{ij} R_{ij}^{-1} f_i f_j}. \quad (39)$$

and the variance in this amplitude is given by

$$\sigma_A^2 = \frac{\sum_{ijkl} R_{ij}^{-1} R_{kl}^{-1} (R_{jl} f_i f_k + 3 \text{ permutations})}{\left(2 \sum_{ij} R_{ij}^{-1} f_i f_j\right)^2}. \quad (40)$$

Since “cosmic variance” is the dominant uncertainty, we calculate the covariance matrix from the correlations of the X-ray map with the simulated CMB maps. Although this implicitly assumes that there are no correlations between the maps, it is a good approximation when the ISW effect is small as discussed in Section 3.5.

The most likely amplitude is found to be $A = -0.008 \pm 0.042$, based on the measured correlation for $\theta < 25^\circ$. (At larger separations the models predict little correlation.) This corresponds to a 95% CL upper limit of $A < 0.061$ (1.65σ), and a 98% CL upper limit of $A < 0.078$ (2.05σ). The amplitudes, A , for different models are summarized in Table 1 along with the X-ray biases inferred from the X-ray map

Table 1
The inferred biases and the expected cross correlation amplitudes $\langle XT(0^\circ) \rangle / \sigma_X \sigma_T$

Ω_A	Implied b_x	A		
		implied b_x	$b_x = 2$	$b_x = 1$
0.0	5.6	0.000	0.000	0.000
0.5	3.9	0.061	0.031	0.016
0.6	3.4	0.077	0.045	0.023
0.7	2.9	0.091	0.063	0.031
0.8	2.4	0.104	0.086	0.043

The biases and amplitudes are taken for a range of models with $\Gamma = 0.25$. The inferred biases and the first column of amplitudes assume that the X-ray fluctuations result solely from large scale structure. The other amplitudes assume a fixed X-ray bias, $b_x = 1$ or $b_x = 2$.

assuming all of the X-ray fluctuations result from large scale structure. Under this assumption, $\Omega_A > 0.5$ is just ruled out at the 95% CL. As discussed above, if there is a significant contribution to the X-rays from Poisson noise, then both the inferred X-ray bias and the predictions for the theoretical correlation are reduced by a factor of $\sigma_{\text{Structure}} / (\sigma_{\text{Structure}}^2 + \sigma_{\text{Poisson}}^2)^{1/2}$. Included in the table are the expected amplitudes for a fixed X-ray bias, $b_x = 1$ or $b_x = 2$. If $b_x = 2$, $\Omega_A > 0.7$ is still ruled out at the 95% CL. In the most pessimistic case, with $b_x = 1$, none of the models can be ruled out.

The analysis we have presented has been conservative in the sense that we have only used the X-ray temperature cross correlation to constrain the models. For nonzero cosmological constant, the spectrum C_l of temperature anisotropies shows a rise at low l which is absent in the COBE spectrum. Inclusion of the latter in our analysis would therefore strengthen our bound on Ω_A . (For example, see Sugiyama & Silk, 1994). We have chosen not to do so because the low l rise is a more model-dependent effect than the X-ray temperature correlation, it being possible to remove the former completely by a tilt in the primordial power spectrum. Nevertheless, a future analysis of a wider class of models should include the C_l information as well.

It is important to search for as many independent constraints on a cosmological constant as possible, because each is subject to different kinds of systematic errors. At present, the best established limits on A come from gravitational lensing studies (Maoz & Rix, 1993; Kochanek, 1996). Kochanek (1996) finds that the lack of observed lensing events implies $\Omega_A < 0.66$ at the 95% confidence level. In addition, recent studies of the deceleration parameter measured in supernovae searches have placed an upper limit of $\Omega_A < 0.51$ at the 2σ level (Perlmutter et al., 1997).

The limit on the cross-correlation amplitude can also be used to constrain open models, where the correlations could be much higher for a given Ω_m , if the X-rays probe at high enough redshifts (Kamionkowski, 1996). The constraints on open models thus are likely to be much more sensitive to assumptions

of the luminosity evolution of the sources than the cosmological constant constraints.

6. Conclusions

Our primary aim in this paper has been to demonstrate how correlations, or the absence of correlations, between the microwave background and deep probes of structure can lead to constraints on cosmological models. The surveys we used were not ideal for this purpose, but even so they resulted in a relevant constraint on the cosmological constant.

Surveys with better angular resolution will improve the signal to noise and thus the confidence with which we can rule out a particular cosmology. With degree scale resolution in both the temperature and X-ray maps, the signal to noise could be improved by 50%. For the linear effect which we are considering here, little is gained by looking at maps with resolution on scales smaller than a degree or two. The CMB photons do not have time to receive a substantial shift from the time varying potential when passing through smaller fluctuations. Since the correlation is restricted to large scales, full sky maps are essential to reduce uncertainties due to accidental correlations.

Future satellite missions, most notably MAP and the Planck Surveyor, will provide full sky maps with sufficient resolution (0.3° and 0.1° , respectively) to be explore this effect fully in the CMB sky. Data from these probes should be available in the next 5–10 years. The prospects for better data for the X-ray sky in the near future are uncertain. The ROSAT survey is sensitive only at lower energies (< 2 keV) and so is likely to be contaminated by galactic and other foregrounds. To search for this effect, ideally one needs a full sky survey of the hard XRB (2–10 keV) which has degree scale resolution and which is sensitive enough to allow an unambiguous subtraction of Poisson fluctuations. Such a survey would also provide a measurement of structure on scales larger than is possible in current optical surveys and would fill in the gap in the power spectrum which lies between the galactic surveys and

the measurements of the microwave background. This kind of mission is now being considered (K. Jahoda, private communication).

One can also consider looking at other possible probes of structure at high red shifts. The formalism for calculating the correlations presented here for X-rays transfers easily to other kinds of probes. Possibilities include surveys of radio galaxies or quasars, or other objects which probe to large redshifts. Galaxy surveys such as the Sloan Digital Sky Survey, which should probe to $z \sim 0.5$, might also be sensitive to this effect and have the added benefit of containing redshift information for the individual sources. An advantage of these probes is that their large scale clustering properties are (or will be) known and the bias implied by a given model can be easily computed. However, if the surface density of these objects is too low (e.g. quasars) then the statistical noise in the cross-correlation function will be large and the effects discussed in this paper will be unobservable.

In this paper we have focused on testing for a cosmological constant, but in fact this is a rather indirect means of testing for Λ . The results we quote are based on a fairly specific model, one which has cold dark matter as well as adiabatic, scale invariant initial fluctuations. It is important to realize however that rather than being sensitive merely to one specific cosmological model, the effect we have considered occurs in any cosmology where the gravitational potential has evolved recently. This includes models that are open or where structures arise from cosmological defects and we are presently working to understand this constraint in these other contexts.

Whatever the cosmological model, the ISW effect reflects important fundamental information relevant to structure formation. The presence of large, empty voids, the apparent lack of mergers and the shapes of clusters of galaxies provide evidence, tentative as yet, that the process of structure formation might be slowing down. If this is the case, then the decay of the linear gravitational potential makes a late time ISW effect inevitable and offers an important observation to confront these other clues about how structures formed in the universe.

Acknowledgements

We thank Elihu Boldt and Jim Peebles for useful discussions. The HEAO1 A2 data and map generating software were kindly provided to us by Keith Jahoda. Much of the data analysis was done at Princeton University and we thank Ed Groth for software and computing support. This work was supported in part by NASA grant #NAG 5-3015, NSF grant #PHY-9222952, and the Monell Foundation.

References

- Allen, J.S., Jahoda, K., & Whitlock, L.A., 1994, *Legacy* 5, 27.
- Andreani, P. & Cristiani, S., 1992, *ApJ*, 398, L13.
- Bahcall, N., 1996, in: *Astrophysical Quantities*, ed. A. Cox (AIP, New York, NY).
- Banday, A.J., Gorski, K.M., Bennett, C.L., Hinshaw, G., Kogut, A., & Smoot, G.F., 1996, *ApJ*, 468, L85.
- Banday, A.J., Gorski, K.M., Bennett, C.L., Hinshaw, G., Kogut, A., Lineweaver, C., Smoot, G.F., & Tenorio, L., 1997, *ApJ*, 475, 393.
- Bennett, C.L., et al., 1996a, *ApJ*, 464, L1.
- Bennett, C.L., Leisawitz, D., & Jackson, P.D., 1996b, COBE Ref. Pub No. 96-B (NASA/GSFC, Greenbelt, MD).
- Boldt, E., 1987, *PhR*, 146, 215.
- Bond, J.R. & Efstathiou, G., 1987, *MNRAS*, 226, 655.
- Boughn, S.P., 1998, *ApJ*, in press, astro-ph/9709077.
- Boughn, S.P. & Jahoda, K., 1993, *ApJ*, 412, L1.
- Boyle, B.J., Shanks, T., Georgantopoulos, I., Stewart G.C., & Griffiths, R.E., 1994, *MNRAS*, 271, 639.
- Bunn, E.F. & White, M., 1997, *ApJ*, 480, 6.
- Carrera, F.J., et al., 1993, *MNRAS*, 260, 376.
- Carrera, F.J., Fabian, A.C., & Barcons, X., 1997, *MNRAS*, 285, 820.
- Chen, L.W., Fabian, A.C., Warwick, R.S., Branduardi-Raymont, G., & Barber, C.R., 1994, *MNRAS*, 266, 846.
- Comastri, A., Setti, G., Zamorani G., & Hasinger, G., 1995, *A&A*, 296, 1.
- Cress, C.M., Helfand, D.J., Becker, R.H., Gregg, M.D., & White, R.H., 1996, *ApJ*, 473, 7.
- Crittenden, R.G. & Turok, N., 1996, *PhRvL*, 76, 575.
- Efstathiou, G., Bond, J.R., & White, S., 1992, *MNRAS*, 258, 1p.
- Efstathiou, G., 1996, in: *Les Houches Lectures*, eds. R. Schaeffer, J. Silk, M. Spiro, & J. Zinn-Justin (Elsevier, Amsterdam), p. 133.
- Gorski, K.M., Ratra, B., Sugiyama, N., & Banday, A., 1995, *ApJ*, 444, L65.

- Gregory, P.C. & Condon, J.J., 1991, *ApJS*, 75, 1011.
- Groth, E.J. & Peebles, P.J.E., 1977, *ApJ*, 217, 385.
- Gunderson, J., et al., 1995, *ApJ*, 443, L57.
- Hasinger, G., Burg, R., Giacconi, R., Hartner, G., Schmidt, M., Trumper, J., & Zamorani, G., 1993, *A&A*, 275, 1.
- Jahoda, K. & Mushotzky, R., 1989, *ApJ*, 346, 638.
- Jahoda, K., 1993, *AdSpR*, 13, No. 12, 231.
- Kamionkowski, M., 1996, *PhRvD*, 54, 4169.
- Kochanek, C., 1996, *ApJ*, 466, 638.
- Kneissl, R., Egger, R., Hasinger, G., Soltan, & Trumper, J., 1997, *A&A*, 320, 685.
- Lahav, O., Piran, T., & Treyer, M., 1997, *MNRAS*, 284, 499.
- Loan, A.J., Wall, J.V., & Lahav, O., 1997, *MNRAS*, 286, 994.
- Madau, P., Ghisellini, G., & Fabian, A.C., 1994, *MNRAS*, 270, L17.
- Maoz, D. & Rix, H., 1993, *ApJ*, 416, 425.
- Miyaji, T., 1994, Ph. D. Thesis, University of Maryland.
- Miyaji, T., Lahav, O., Jahoda, K., & Boldt, E., 1994, *ApJ*, 434, 424.
- Netterfield, C.B., Devlin, M.J., Jarosik, N., Page, L., & Wollack, E.J., 1997, *ApJ*, 474, 47.
- Perlmutter, S., et al., 1997, *ApJ*, 483, 565.
- Piccinotti, G., Mushotzky, R., Boldt, E., Holt, S., Marshall, F., Serlemitsos, P., & Shafer, R., 1982, *ApJ*, 253, 485.
- Rees, M.J. & Sciama, D.W., 1968, *Natur*, 217, 511.
- Refregier, A., Helfand, D.J., & McMahon, R.G., 1997, *ApJ*, 477, 58.
- Sachs R.K. & Wolfe, A.M., 1967, *ApJ*, 147, 1.
- Scott, D., Silk, J., & White, M., 1995, *Sci*, 268, 829.
- Sicotte, H., 1995, Ph. D. Thesis, Princeton University.
- Soltan, A., Hasinger, G., Egger, R., Snowden, S., & Trumper, J., 1996, *A&A*, 305, 17.
- Soltan, A., Hasinger, G., Egger, R., Snowden, S., & Trumper, J., 1997, *A&A*, 320, 705.
- Sugiyama, N., 1995, *ApJS*, 100, 281.
- Sugiyama, N. & Silk, J., 1994, *PhRvL*, 73, 509.
- Tully, R.B., 1988, *Nearby Galaxies Catalog* (Cambridge University Press, Cambridge).
- White, M. & Bunn, E.F., 1995, *ApJ*, 450, 477.
- White, R.A. & Stemwedel, S.W., 1992, in: *Astronomical Data Analysis Software and Systems I*, eds. D.M. Worrall, C. Biemesderfer, & J. Barnes (ASP, San Francisco, CA), p. 379.
- Zdziarski, A.A., Zycki, P.T., & Krolik, J.H., 1993, *ApJ*, 414, L81.